

Layer-by-Layer Epitaxy of Porphyrin–Ligand Fe(II)-Fe(III) Nanoarchitectures for Advanced Metal–Organic Framework Growth

Zishu Wang,[□] Kai Qian,[□] Murat Anil Öner,[□] Peter S. Deimel, Yan Wang, Shuai Zhang, Xiaoxi Zhang, Vishal Gupta, Juan Li, Hong-Jun Gao, David A. Duncan, Johannes V. Barth, Xiao Lin, Francesco Allegretti,* Shixuan Du, and Carlos-Andres Palma*



Cite This: *ACS Appl. Nano Mater.* 2020, 3, 11752–11759



Read Online

ACCESS |



Metrics & More



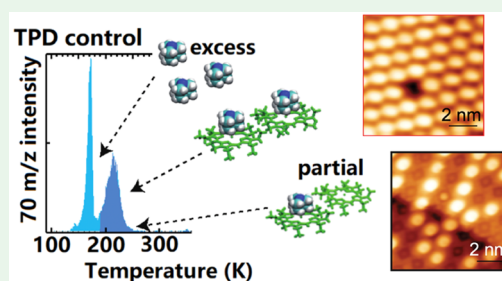
Article Recommendations



Supporting Information

ABSTRACT: Precisely layered molecular heterostructures are promising but still largely unexplored materials, with the potential to complement and enhance the scope of two-dimensional heterostructures. The controlled epitaxial growth of vertically stacked molecular layers connected through tailored linkers, can lead to significant development in the field. Here, we demonstrate that sequential assembly of prototypical iron porphyrins and axial ligands can be steered via temperature-programmed desorption, and monitored by mass spectrometry and by high-resolution atomic force microscopy under ultrahigh vacuum conditions. Complementary photoelectron spectroscopy analysis delivers chemical insight into the formation of layer-by-layer nanoarchitectures. Our temperature-directed methodology outlines a promising strategy for the in vacuo fabrication of precisely stacked, multicomponent (metal–organic) molecular heterostructures.

KEYWORDS: *bottom-up self-assembly, molecular architectures, scanning tunneling microscopy, scanning probe microscopy, thermal desorption spectroscopy, directed self-assembly, photoemission, three-dimensional atomically-precise fabrication*



INTRODUCTION

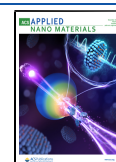
Directed self-assembly of molecular architectures in three dimensions (3D) is a fundamental process of complex matter.^{1–3} Its control is crucial for the fabrication of hybrid organic–inorganic molecular heterostructures, which are promising candidates for modular, integrated electronic nanodevices.^{4–16} While self-assembly in two dimensions (2D) is well-established, research to achieve epitaxial deposition of truly precise supramolecular arrays stacking into the third dimension, is still in its infancy. Popular strategies for 3D-directed self-assembly at well-defined interfaces include templated growth^{17–29} and solution layer-by-layer (LbL) growth.^{30–32} The general LbL approach³³ for tailored reticular architectures is highly appealing due to the possibility of incorporating different molecular species at each stratum,¹³ thereby approaching biological complexity. However, precision 3D growth of heterostructures is largely limited by the understanding of complexation kinetics and diffusion rates of the individual molecular species, and by the ample self-assembly parameter space, which cannot necessarily guarantee stoichiometrically layered materials. Progress has mostly relied on trial-and-error parameter (temperature, pressure, and number of molecules) optimization with limited thermodynamic and single-molecule precision. The use of solvents can be circumvented under UHV conditions; yet new variables arise, for example, in physical vapor deposition, that may affect reproducibility at the atomic level.^{34,35} Here, we show that LbL

growth in ultrahigh vacuum (UHV) environments is possible, whereby promising kinetic and molecular control of multicomponent organic architectures can be exerted via temperature control, as elucidated by temperature-programmed desorption mass spectrometry^{36–40} (TPD-MS), complemented by scanning probe microscopies (SPM) and X-ray photoelectron spectroscopy (XPS). In particular, TPD-MS offers a new paradigm to monitor and steer the monolayer-by-monolayer assembling process, and tailor sophisticated functional heterostructures. An early example of complexation between metal–organic building blocks under UHV conditions came from Williams et al.,⁴¹ who demonstrated that, at 123 K, 1,4-diazabicyclo[2.2.2]octane (DABCO)–metalloporphyrin complexes could be formed on the Ag(100) surface. Decomplexation was monitored after thermal annealing at 298 K. Stimulated by the possibility of achieving stoichiometric and structural control of complex matter by desorption, we apply TPD-MS to identify the thermal conditions at which monolayers of porphyrins can be prepared, and complexation

Received: August 18, 2020

Accepted: November 9, 2020

Published: November 25, 2020



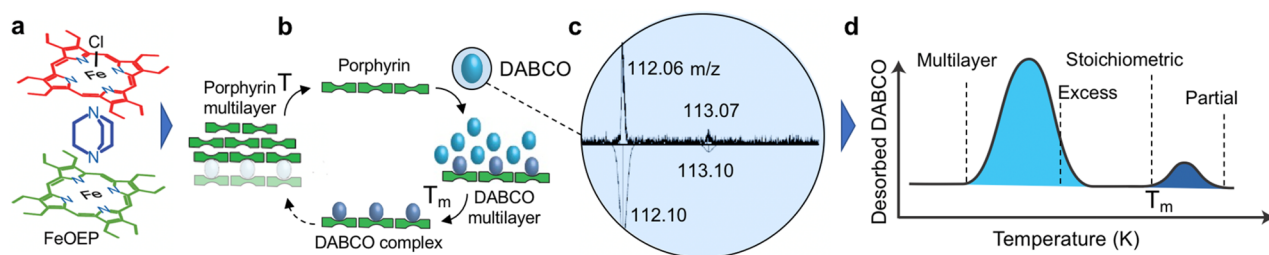


Figure 1. Schematics of layer-by-layer (LbL) epitaxy of a three-component architecture. (a) Vertical stacking of dechlorinated FeOEP (green), DABCO (blue), and FeOEP-Cl (red) defining one type of Fe(II)-Fe(III) heterostructure. (b) General approach for LbL assembly via temperature control, consisting of deposition and annealing-desorption cycles. (c) ToF-MS of DABCO sublimed at 363 K from precursor DABCO-CuCl (above) and the simulated spectrum (below). (d) Temperature-controlled desorption approach: An excess of linker molecules is deposited onto a dechlorinated porphyrin monolayer (FeOEP in green, panels a,b). The molecules are subsequently desorbed through thermal annealing. TPD-MS monitors and identifies the temperature required to obtain full complexation. In principle, a near-to-stoichiometric layer may be prepared by thermal annealing above the excess peak (light blue) to temperature T_m and just below the onset of the target stoichiometry peak (dark blue).

with DABCO efficiently steered. We employ organic molecular beam epitaxy (OMBE) to sequentially deposit metalloporphyrins and model organic linkers onto a Au(111) substrate, and TPD-MS to identify the conditions under which the targeted metal-ligand coordination complexes form by monitoring desorption temperatures (Figure 1). By way of an example, we consider the deposition of a single layer of iron(III) octaethylporphyrin chloride (FeOEP-Cl), followed by its dechlorination on a metal substrate,⁴² the subsequent ligation of a second layer of a 1,4-diazabicyclo[2.2.2]octane (DABCO) linker, and then a third layer of FeOEP-Cl species. XPS enables one to follow the associated chemical changes in the Fe $2p_{3/2}$ signal, attributed to Fe(III)-Cl, Fe(II), and Fe(II)-DABCO.⁴³⁻⁴⁵ We show that the deposition of the outermost iron porphyrin layer does not affect the composition of the two layers underneath, thus highlighting the potential of the method for controlling 3D growth of mixed-valence magnetic Fe(II)-DABCO-Fe(III) nanomaterials (Figure 1a). Our work thus outlines an important avenue to LbL growth of well-defined, multicomponent complex matter. We expect our methodology to pave the way toward multicomponent molecular arrays, and stimulate paradigmatic molecularly precise applications.

EXPERIMENTAL SECTION

For XPS and TPD-MS measurements, DABCO-CuCl and FeOEP-Cl (Sigma-Aldrich) precursors were sublimed at 385 K and 493 K, respectively (pressure $\sim 1 \times 10^{-10}$ mbar, 10 cm sample-crucible distance; 4–30 min deposition, refer to the text and the Supporting Information) onto Au(111) held at ~ 85 K. DABCO-CuCl was chosen as a DABCO precursor due to its lower vapor pressure. Freshly sputtered and annealed Au(111) over a mica support was employed as a substrate (Georg Albert PVD substrates, Germany) for TPD-MS, XPS, and FM-AFM studies, whereas a Au(111) single crystal (MaTeck) was used for the scanning tunneling microscopy (STM) investigations. Frequency-modulated atomic force microscopy (FM-AFM) data were acquired in constant frequency mode (RHK Technology), employing Nanoprobe PPP cantilevers driven at ~ 0.8 MHz and 5–10 mV excitation amplitude at a base pressure of $\sim 1 \times 10^{-8}$ mbar. UHV STM (Omicron) and XPS (nonmonochromatized Mg $K\alpha$ source with the main photon line at 1253.6 eV; SPECS PHOIBOS 100 CCD analyzer for photoelectron detection) data were collected in two different experimental chambers at 80–90 K. Because of detectable radiation damage, a new sample was prepared after ~ 50 min of continuous X-ray exposure, and each XP spectrum was optimized for fast acquisition (~ 10 min). In general, XPS experiments were repeated detecting photoelectrons at normal emission (NE, $\theta_e = 0^\circ$) and grazing emission (GE, $\theta_e = 70^\circ$). TPD was employed to

calibrate the sublimation times and to desorb weakly bound excess layers for advanced assembly protocols. The TPD spectra were acquired in the same chamber used for XPS at a base pressure of 8×10^{-11} mbar, with a quadrupole mass spectrometer enclosed within a copper cap and the sample positioned close to a millimeter from the cap aperture.^{46,47} The temperature was varied linearly via radiative heating from a tungsten filament placed close to the back of the sample, whereby a PID controller was used (Schlichting Physikalische Instrumente HS 130). A heating rate of 0.5 K s^{-1} was employed in the TPD measurements throughout this work. To prevent artifacts due to the above-mentioned radiation damage, TPD-MS spectra were recorded solely from surfaces not previously exposed to X-ray radiation. ToF-MS (Kore Technology) was carried out at a base pressure of 1×10^{-9} mbar with an electron-impact analyzer working at 10 eV and 200 μA emission current. The detector collects molecules for 15 min employing 300 μs pulsed cycles. TPD-MS in conjunction with XPS was employed to calibrate DABCO uptake on Au(111) (Figure S1). First, multilayers were deposited (Figure S1c), showing a multilayer peak signal at 191.5 K, which is typical for the desorption of multilayer small organic molecules at surfaces. Sublimation times were reduced until a single TPD desorption peak maximum is observed (263 K, Figure S1c, inset). No traces of chlorine or copper from the chosen DABCO-CuCl precursor were found, and the N:C ratio (2.5:6; ideal, 2:6) and ToF-MS data in Figure 1c further indicate that intact DABCO is adsorbed. The XPS spectra were calibrated in binding energy using the Au $4f_{7/2}$ core level at a binding energy of 84.0 eV. A polynomial and/or Shirley template background was subtracted, and the spectra were fitted with Gaussian-Lorentzian line shapes via the CasaXPS software (Casa Software Ltd., version 2.3.23PR1.0). STM data were analyzed with the Gwyddion software (version 2.45).⁴⁸ STM and AFM unit cells were postcorrected by HOPG and by Au(111), respectively.

RESULTS AND DISCUSSION

Throughout the work, TPD-MS serves to calibrate sublimation times and to desorb weakly bound excess layers, while XPS helps monitor the chemical changes of the FeOEP-Cl layers. The initial step to prepare the first porphyrin layer is to deposit an excess of FeOEP-Cl (Figure 2a–d) onto Au(111) held at 85 K. An analysis of the Fe $2p_{3/2}$ XP spectrum reveals a main broad component centered at ~ 710 eV, which is ascribed to an iron multiplet structure⁴⁹ (Figure 2a). The N:C intensity ratio amounts to about 1:8 (stoichiometric 1:9, Figure 2b, N 1s 398.2 eV; Figure S2, C 1s 284.6 eV) and the relative C 1s to Cl 2p intensity at 197.8 eV to roughly 35:1 (stoichiometric 36:1) after we corrected for the respective photoionization cross sections. TPD-MS is subsequently employed to guide the formation of a tightly packed dechlorinated monolayer. The TPD spectra of Figure 2c show the desorption of FeOEP-Cl

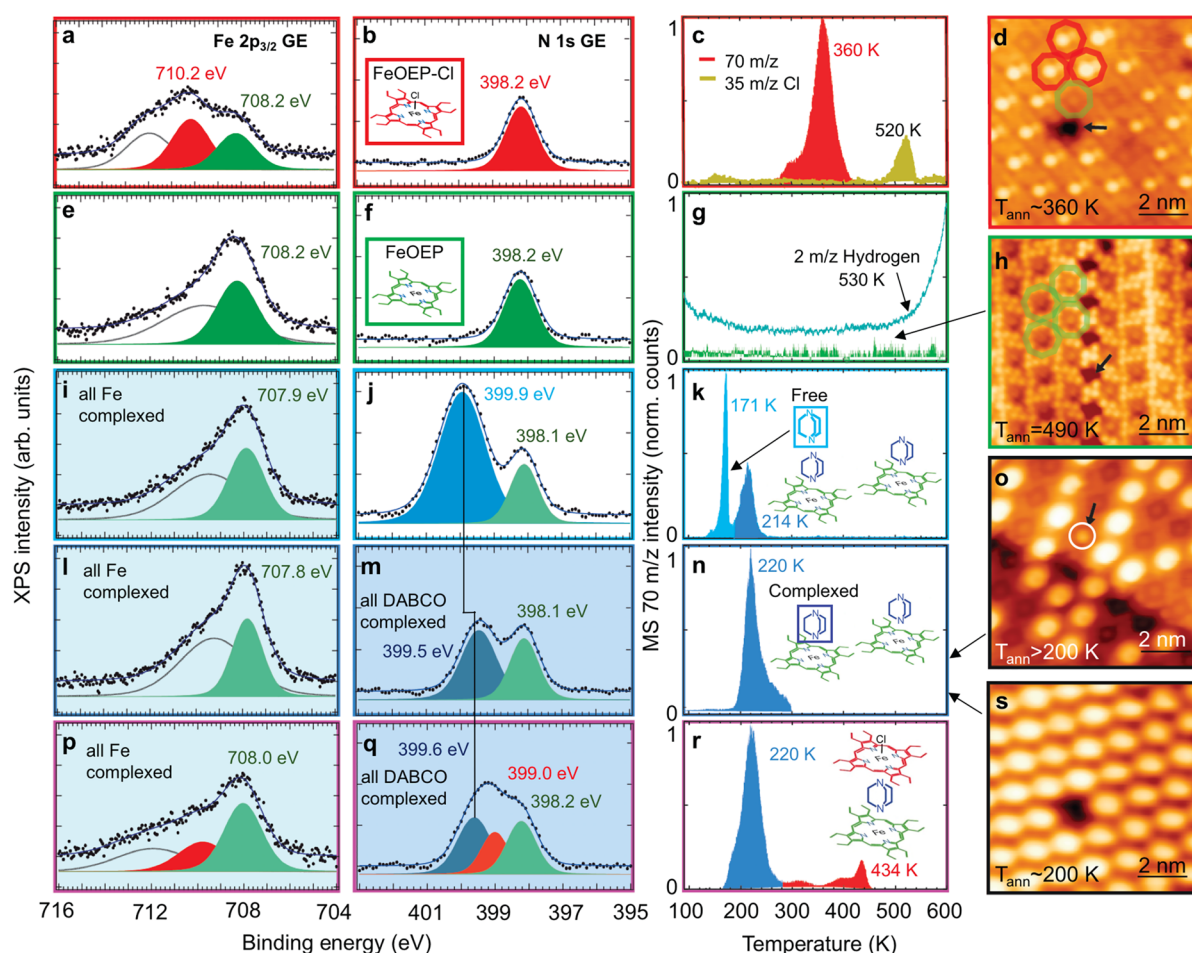


Figure 2. Temperature-directed LbL growth on Au(111) monitored by XPS (recorded at $T = 85$ K), TPD-MS, and STM. (Row a–d) FeOEP–Cl on Au for a coverage beyond saturated monolayer concentration and corresponding annealing. (Row e–h) A single monolayer of FeOEP on Au is formed after annealing to desorb the multilayer and to dechlorinate the porphyrin molecules. (Row i–k) FeOEP monolayer covered by DABCO layers comprising two different bonding configurations identified by TPD-MS. (Row l–n) A single layer of complexed DABCO on FeOEP is formed after TPD-monitored annealing to 185 K. (o, s) STM data showing: a discontinuous DABCO layer upon further removal of DABCO in (o) and a full DABCO monolayer with a single molecule missing in (s). (Row p–r) Further deposition of a single layer of FeOEP–Cl results in intact FeOEP–DABCO signals coexisting with FeOEP–Cl, tentatively assigned to a FeOEP–DABCO/FeOEP–Cl stacking. (Column a,e,i,l,p) Background subtracted grazing emission (GE) XPS of the Fe $2p_{3/2}$ region and (columns b,f,j,m,q) GE XPS of the N $1s$ region. (Column c,g,k,n,r) TPD-MS at 0.5 K s^{-1} monitoring the 70 m/z channel for DABCO and FeOEP fragments. The 35 m/z Cl channel and 2 m/z hydrogen channel are also monitored in (c) and (g), respectively. Colored XPS fits and TPD data represent our interpretation of the peaks, added as a guide to the eye: FeOEP–Cl in various environments (red), FeOEP adsorbed on Au (green), FeOEP complexed (turquoise), heterogeneous DABCO layer on FeOEP (cyan), and DABCO complexed (blue). (Column d,h,o,s) Representative STM data, $V_s = -0.8$ V, $I_s = 300$ pA in (d); and $V_s = -2.0$ V, $I_s = 100$ pA in (h,o,s). Dark and white represent 0 and 5.6 Å apparent STM heights in the false color scale, respectively. Point defects (arrows in d,h) highlight the apparent height differences between strata. Arrow in (o) marks a single chlorinated FeOEP species in the discontinuous FeOEP–DABCO layer.

and chlorine, respectively. Ionization fragments at 70 m/z (corresponding to FeN or C_5H_{10} FeOEP–Cl fragments or a C_4H_8N DABCO electron-impact MS fragment⁵⁰ as verified by ToF-MS) and at 35 m/z (chlorine) were monitored. As depicted in Figure 2c, a FeOEP–Cl desorption maximum at 360 K (red, associated with the desorption of excess molecules in a condensed multilayer) and a dechlorination feature (yellow) with onset at 490 K are observed. Indeed, STM confirms that the porphyrin layer annealed to ~ 360 K (and thus the first TPD peak maximum) is comprised of mainly intact FeOEP–Cl species⁴² (red octagons in Figure 2d).

The data in Figure 2e,f characterize the FeOEP monolayer obtained after annealing of the previous layer at 473 K for 20 min. Longer annealing routines lower than 490 K are employed to avoid dehydrogenation effects^{42,51–53} (see

below), equally resulting in dechlorination as confirmed by the absence of the XPS Cl $2p$ signature (not shown). The Fe $2p_{3/2}$ line displays a clear redistribution of spectral weight to lower binding energy. This signature is indicative of a lower Fe(II) oxidation state,⁵⁴ previously identified as an intermediate-spin state ($S = 1$).^{43–45} The broad Fe $2p_{3/2}$ line shape is attributed to the complex multiplet structure for transition metals with an open shell combined with a laterally inhomogeneous interaction of the adsorbed molecules with the underlying gold surface.⁵⁴ Note that, due to the moderate energy resolution of our measurements (~ 0.9 eV), the qualitative curve-fitting analysis presented in Figure 2 was based on the main discernible components without attempting to fully resolve the details of the multiplet structure. Nevertheless, a clear evolution is observed, irrespective of

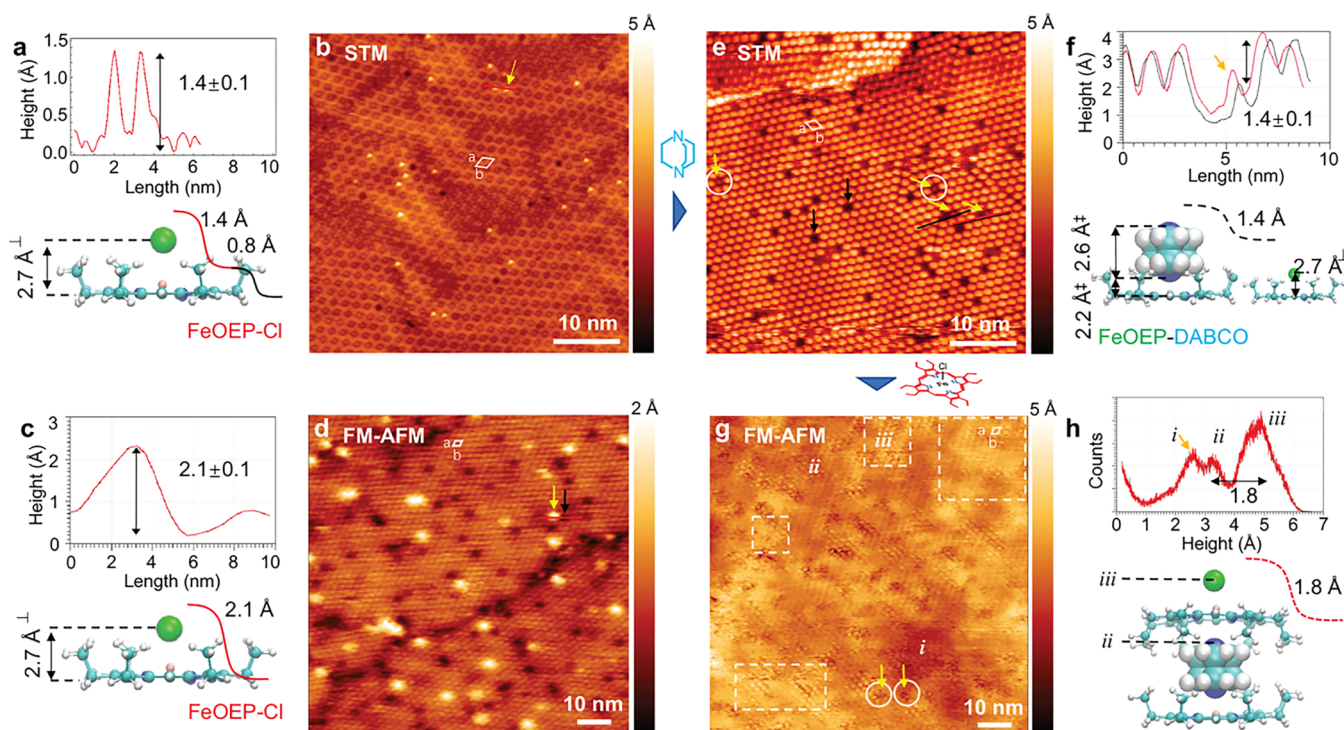


Figure 3. Temperature-directed LbL growth on Au(111) monitored by STM and FM-AFM. (a,b) STM and (c,d) FM-AFM topography data highlighting partial dechlorination into FeOEP (selected remaining Cl atoms indicated by yellow arrows) after deposition of FeOEP–Cl and annealing. Domain boundaries and vacancies are occasionally observed. The feedback (apparent height) profiles in (a) and (c) of 2.2 (1.4 + 0.8) Å and 2.1 Å correspond to Cl distances as measured from nearby vacancies by AFM and STM, respectively ([†]the Cl–porphyrin plane distance has been measured as 2.7 Å and the Cl–Fe distance as 2.2 Å, by single-crystal X-ray diffraction).⁶⁷ Molecular models: N (blue), C (cyan), Fe (pink), and Cl (green). (e,f) STM data after deposition of DABCO and annealing. The apparent DABCO height referenced to a neighboring FeOEP–Cl (f) is 1.4 Å. [‡]The X-ray resolved DABCO–porphyrin plane height is 4.8 Å: 2.6 Å (DABCO size) plus 2.2 Å (DABCO–Fe distance).⁶⁸ (g,h) FM-AFM data after deposition of FeOEP–Cl on top of FeOEP–DABCO, for which three strata (i, ii, iii; see text) can be identified as supported by Figure S5 (see text), and model of the possible heterostructure. Imaging parameters (b,e) $T = 77$ K, $I_t = 100$ pA, $U_t = -2$ V, $a = b = (1.55 \pm 0.1)$ nm, median row background subtraction; (d) $T = 293$ K, $a = b = (1.6 \pm 0.1)$ nm, $f = 868.057$ kHz, $\Delta f = -10$ Hz, median row background subtraction; and (g) $T = 293$ K, $a = b = (1.5 \pm 0.1)$ nm, $f = 868.044$ kHz, $\Delta f = -10$ Hz quadratic background subtraction.

the detailed substructure of the Fe $2p_{3/2}$ core level. The TPD of this FeOEP monolayer (Figure 2g) shows thermal stability until 530 K (at 0.5 K s^{-1}) where dehydrogenation reactions at the periphery of the porphyrin macrocycle set in,^{42,51–53} resulting in hydrogen desorption. STM data (Figure 2h) confirm that >99% of the molecules undergo dechlorination upon annealing. Green octagons highlight the centers of the FeOEP molecules, surrounded by eight protruding ethyl moieties that are hexagonally arranged (Figure S3).^{42,45,51,53}

In the next step, DABCO is sublimed at 385 K and deposited on top of the FeOEP monolayer, aiming at the target FeOEP–DABCO complexed monolayer (Figure 2i–k). XPS reveals that the dominant Fe $2p_{3/2}$ low binding energy component becomes sharper and distinctly shifts to lower binding energies (from 708.2 to 707.9 eV, Figure 2i; cf. also Figure S2c). One interpretation of this sharpening is that the iron(II) intermediate-spin-like configuration is weakened,⁴⁵ transformed into low spin typical of a hexacoordinated ferrous ion⁵⁵ (e.g., with DABCO and the underlying Au(111) substrate^{56,57}) or related coordination sphere distortion, as reported in diverse studies.^{45,58,59} Indeed, high-resolution photoemission studies of iron phthalocyanine on Au(111) have pointed out the ability to tune the spin state of the iron centers by ligand coordination, leading to a distinct sharpening of the Fe $2p_{3/2}$ core level line in the low-spin configuration.^{59,60} Concurrently, a weakening of the coupling of the metal

complex to the substrate upon ligand coordination is also expected to contribute to a narrowing of the core-level line.^{54,57} Conversely, strongly distorted macrocycles have been associated with high-spin ($S = 2$) Fe(II).^{61–63} The binding energy associated with the DABCO N 1s core level (399.9 eV) is similar to the value for a condensed film on bare Au(111); see Figure 2j and Figure S1b. Again, TPD-MS is employed to both rationalize and monitor the hybrid layer. The data reproduced in Figure 2k reveal the existence of two different states for DABCO: a weakly bound fraction desorbing at 171 K and a more strongly bound species desorbing at 214 K. The sharp TPD peak at 171 K is assigned to desorption of DABCO multilayers on FeOEP. A similar component is also detected for DABCO multilayers condensed on the pristine gold surface (191 K, Figure S1c). The second desorption peak, at 214 K, is assigned to DABCO directly coordinated to the central iron atoms upon complexation, which explains the increased binding strength. Interestingly, the barrier for desorption of this DABCO layer (214 K, Figure 2k) is lower than that of DABCO layers in direct contact with the bare gold substrate (263 K, Figure S1c). A weak DABCO–FeOEP interaction can be attributed to the large distance⁶⁴ between DABCO and the octaethyl adsorption pocket (i.e., H···H distances amount to 3.6 Å between DABCO and the octaethyls in Figure S3b).

TPD is subsequently employed to thermalize DABCO for homogeneous complexation, while desorbing the weakly

bound 171 K component on FeOEP (“TPD-control”), as schematically depicted in Figure 1b,d. Accordingly, after TPD-monitored annealing to 185 K, the Fe $2p_{3/2}$ signal further sharpens, and the N 1s signal associated with DABCO shifts down to 399.5 eV (Figure 2l,m). The TPD spectrum recorded after this additional annealing step now exhibits a single desorption peak (Figure 2n) which confirms that only the more strongly bound DABCO species, assigned to DABCO coordinated to FeOEP, remains. STM investigations of the DABCO–porphyrin system annealed at >200 K reveal a slight loss of ligated DABCO, indicating that complexation is achieved between the desorption peak onset at ~190 K and its cessation below ~300 K (Figure 2o). A full DABCO monolayer can be prepared at ~200 K (Figure 2s). Analysis of the N 1s signals in Figure 2m indicates a peak area ratio of 1.3:1, setting an upper bound on the DABCO:Fe coverage of approximately 2.6:1 at 185 K. The deviation from the expected 1:1 coverage can be understood partly due to the differences between electron attenuation of the two components at GE and partly due to the presence of secondary DABCO species. Regarding the electron attenuation, semiquantitative XPS mandates a careful modeling of each layer of the system.⁶⁵ To understand the influence of the secondary DABCO species, the system is annealed close to 215 K and the coverage is reduced to the expected 1:1 (Figure S2a, orange curve). At these annealing temperatures, the Fe $2p_{3/2}$ signal is no longer indicative of DABCO:FeOEP complexation (Figure S2c, orange curve). This can be rationalized by DABCO adsorption on defects (cf. density functional tight binding⁶⁶ modeling, Figure S3c) or mobile DABCO under low-coverage measuring conditions.

In the final step, we deposit a submonolayer of FeOEP–Cl as a third layer on top of the FeOEP–DABCO system that was grown under TPD-control (Figure 2p–r). A notable difference is that the N 1s component related to the porphyrin shifts to a higher binding energy, 399.0 eV (red, Figure 2q), indicative of the decoupling from the metal surface. The DABCO complex on FeOEP remains intact as judged by the associated N 1s line being stable at 399.6 eV. As TPD-control guarantees at least a complete, intact FeOEP–DABCO bilayer, the subsequently deposited FeOEP–Cl must adsorb on top of it (see Figure 3). Despite these observations, the TPD of the trilayer shows a prominent DABCO signal component remaining constant at ~220 K (Figure 2r). One interpretation is that DABCO desorbs from regions not covered by FeOEP–Cl, consistent with a submonolayer of FeOEP–Cl being deposited. Thus, the new signals between 300 K and 434 K in Figure 2r are assigned to both DABCO and FeOEP–Cl desorbing from multiple configurations enabled by the deposition of the third layer of FeOEP–Cl.

SPM techniques serve to evaluate the epitaxial precision of the layers when emulating the conditions previously identified by TPD-control. Both FM-AFM and STM (Figure 3a–d) are employed to characterize the first layer after the deposition of FeOEP–Cl and annealing for partial dechlorination, keeping a few chlorine atoms as a reference for analyzing the data. Selected data with nanoscale domains and defects further facilitate the interpretation of the SPM, via apparent heights corresponding to different molecular strata species. Note that encountering high-quality single-domain monolayers with minimal defects is also common (Figure S4a). The similar STM and FM-AFM topography can be assigned to the FeOEP ordered assembly characterized by vectors $a = b = (1.55 \pm 0.1)$

nm (STM), $a = b = (1.6 \pm 0.1)$ nm (FM-AFM) and by angle $(a,b) = 60^\circ$. Different types of vacancies and chlorinated FeOEP–Cl species are discerned (Figure 3b,d). In FM-AFM data, the lateral broadening of vacancies and chlorinated defects varies due to tip effects, a phenomenon also observed in the STM data (Figure S4b). The apparent distance between the chlorine atoms and the porphyrin plane as measured from vacancies amounts to 2.2 Å in the STM and 2.1 Å in the FM-AFM data, respectively (Figure 3a–d). The measured 2.2 Å corresponds to the 1.4 Å chlorine contribution plus a ~0.8 Å contribution stemming from the apparent height of the backfolded octaethyl units, measured against a FeOEP vacancy corresponding to the Au(111) substrate. These apparent heights serve to identify different molecular layers. It is worth mentioning that the reported Cl–porphyrin plane distance, as determined from single-crystal X-ray diffraction, is 2.7 Å,⁶⁷ up to 0.6 Å above the SPM estimation.

The FeOEP monolayer after DABCO deposition is depicted in Figure 3e,f. Here, the STM apparent height of the deposited DABCO (Figure 3e,f) varies with respect to different kinds of vacancies (shown by the black arrow in Figure 3e). While it is challenging to verify the identity of such vacancies, nonvacant defects (white circles and yellow arrows in Figure 3e) can be plausibly assigned to occasional chlorinated FeOEP–Cl species. The apparent height of DABCO with respect to a neighboring chlorinated FeOEP–Cl defect (black and red profiles in Figure 3e) amounts to 1.4 Å (Figure 3f). This corresponds to a 0.7 Å deviation from the reported difference in heights between Cl–porphyrin and DABCO–porphyrin (see Figure 3f),^{67,68} consistent with the SPM height underestimation in Figure 3a–d. Thus, chlorinated defects serve as a reference for the interpretation of multilayered SPM data. Accordingly, upon deposition of a submonolayer of FeOEP–Cl, three regions are identified (Figure 3g,h). FM-AFM height data are strongly influenced by tip–molecule–substrate interactions and particularly change at interfaces and boundaries, where polarization effects are strongest.⁶⁹ Thus, the DABCO region (ii, Figure 3g,h) is identified in FM-AFM data employing the chlorinated defects (region i) as reference (circles in Figure 3g and Figure S5). Importantly, repeated attempts to image the sample after deposition of the third molecular layer by STM were unsuccessful, presumably because of tip contamination effects in the presence of a multilayered architecture. Therefore, FM-AFM becomes a key microscopy tool capable of studying these multilayered architectures as shown in Figure 3g, where nanocrystalline epitaxial domains, with $a = b = (1.5 \pm 0.1)$ nm and angle (a,b) of 60° are observed, notably similar to those of the underlying FeOEP–DABCO template. The height histogram (Figure 3h) of the top molecular stratum (region iii, white boxes) admits a 1.8 Å height difference from the DABCO layer (region ii). This apparent distance can be tentatively assigned to the expected height of FeOEP–Cl measured in Figure 3a–d, in agreement with an epitaxial third layer assembly. Notwithstanding these observations, a third layer stemming from DABCO layers cannot be unambiguously excluded. Multiple DABCO layers are unlikely to adopt an identical 2D mesh as the underlying FeOEP–DABCO bilayer under the imaging conditions, due to relatively weak DABCO–DABCO interactions. Instead, different height regions, together with the comparative XPS and TPD studies in Figure 2 and profile analysis in Figure S5, support the formation of nanoscopic

domains plausibly accommodating Fe(II)-Fe(III) based FeOEP–DABCO–FeOEP–Cl heterostructures.

CONCLUSION

In summary, we have introduced a fabrication protocol toward controlled engineering of interfacial molecular heterostructures, monitored by a combination of temperature-programmed desorption, mass spectrometry, photoemission spectroscopy, and high-resolution scanning probe microscopy under ultrahigh vacuum conditions. The scheme is exemplified by the sequential layer-by-layer assembly of an FeOEP–DABCO architecture on Au(111) steered via in situ complexation, and supported by evidence for nanoscopic domains of FeOEP Fe(II), DABCO, and FeOEP–Cl Fe(III) heterostructures. Although the stability and long-range epitaxy of the latter remain to be explored in more detail, we expect that our temperature-directed methodology along with the use of carefully selected building blocks will enable precision layer-by-layer growth of van der Waals molecular heterostructures and metal–organic architectures. In particular, suitable linkers ensuring heteromolecular (AB) interactions stronger than homomolecular (AA, BB) interactions, that is, with desorption temperatures T_{AB} higher than T_{AA} and T_{BB} , are desirable to improve and refine the temperature-controlled procedure for multilayer growth. Our approach outlines a route to achieve the monolayer-by-monolayer assembly of sophisticated multi-component frameworks, opening novel avenues for the precise engineering of complex matter down to the molecular level.

ASSOCIATED CONTENT

Supporting Information

The Supporting Information is available free of charge at <https://pubs.acs.org/doi/10.1021/acsnm.0c02237>.

XPS and TPD of DABCO on gold and overview STM data; comparative STM, FM-AFM data and molecular modeling (PDF)

AUTHOR INFORMATION

Corresponding Authors

Francesco Allegretti – Physics Department E20, Technical University of Munich, Garching 85748, Germany;

orcid.org/0000-0001-6141-7166;

Email: francesco.allegretti@ph.tum.de

Carlos-Andres Palma – Institute of Physics, Chinese Academy of Sciences, Beijing 100190, P. R. China; Physics Department E20, Technical University of Munich, Garching 85748, Germany; Department of Physics & IRIS Adlershof, Humboldt-Universität zu Berlin, Berlin 12489, Germany;

orcid.org/0000-0001-5576-8496; Email: palma@iphy.ac.cn

Authors

Zishu Wang – Institute of Physics, Chinese Academy of Sciences, Beijing 100190, P. R. China; School of Physical Sciences, University of Chinese Academy of Sciences, Beijing 100049, P.R. China

Kai Qian – Institute of Physics, Chinese Academy of Sciences, Beijing 100190, P. R. China; School of Physical Sciences, University of Chinese Academy of Sciences, Beijing 100049, P.R. China

Murat Anil Öner – Physics Department E20, Technical University of Munich, Garching 85748, Germany

Peter S. Deimel – Physics Department E20, Technical University of Munich, Garching 85748, Germany

Yan Wang – Institute of Physics, Chinese Academy of Sciences, Beijing 100190, P. R. China; School of Physics, Beijing Institute of Technology, Beijing 100081, P.R. China

Shuai Zhang – Institute of Physics, Chinese Academy of Sciences, Beijing 100190, P. R. China; School of Physical Sciences, University of Chinese Academy of Sciences, Beijing 100049, P.R. China

Xiaoxi Zhang – Institute of Physics, Chinese Academy of Sciences, Beijing 100190, P. R. China; School of Physical Sciences, University of Chinese Academy of Sciences, Beijing 100049, P.R. China

Vishal Gupta – Institute of Physics, Chinese Academy of Sciences, Beijing 100190, P. R. China

Juan Li – Institute of Physics, Chinese Academy of Sciences, Beijing 100190, P. R. China; Advanced Research Institute for Multidisciplinary Science, Beijing Institute of Technology, Beijing 100081, P.R. China

Hong-Jun Gao – Institute of Physics, Chinese Academy of Sciences, Beijing 100190, P. R. China; School of Physical Sciences, University of Chinese Academy of Sciences, Beijing 100049, P.R. China; CAS Key Laboratory of Vacuum Physics, Chinese Academy of Sciences, Beijing 100190, P.R. China; orcid.org/0000-0002-6766-0623

David A. Duncan – Physics Department E20, Technical University of Munich, Garching 85748, Germany; Diamond Light Source, Didcot OX11 0QX, United Kingdom;

orcid.org/0000-0002-0827-2022

Johannes V. Barth – Physics Department E20, Technical University of Munich, Garching 85748, Germany;

orcid.org/0000-0002-6270-2150

Xiao Lin – Institute of Physics, Chinese Academy of Sciences, Beijing 100190, P. R. China; School of Physical Sciences, University of Chinese Academy of Sciences, Beijing 100049, P.R. China; CAS Key Laboratory of Vacuum Physics, Chinese Academy of Sciences, Beijing 100190, P.R. China

Shixuan Du – Institute of Physics, Chinese Academy of Sciences, Beijing 100190, P. R. China; School of Physical Sciences, University of Chinese Academy of Sciences, Beijing 100049, P.R. China; CAS Key Laboratory of Vacuum Physics, Chinese Academy of Sciences, Beijing 100190, P.R. China; orcid.org/0000-0001-9323-1307

Complete contact information is available at:

<https://pubs.acs.org/doi/10.1021/acsnm.0c02237>

Author Contributions

□Z.W., K.Q., and M.A.O. contributed equally.

Funding

We acknowledge support from the NSFC China (nos. 51325204, 61622116, 21661132006, 21902012, and 11974403 and Sino-German project no. 51761135130), the CAS Bureau of Frontier Sciences and Education no. QYZDB-SSW-SLH038, the Deutsche Forschungsgemeinschaft (DFG) through the TUM International Graduate School of Science and Engineering (IGSSE, GSC 81), the Munich Centre for Advanced Photonics, the priority program COORNETs (SPP1928), the ERC Horizon 2020 FET Project 2D-Ink (no. 664878), and the Alexander von Humboldt Foundation. We thank Prof. Peter Feulner for methodological support in TPD-MS, together with José D. Cojal-González and Jürgen P. Rabe for discussions.

Notes

The authors declare no competing financial interest.

REFERENCES

- (1) Fujita, M. Metal-directed self-assembly of two- and three-dimensional synthetic receptors. *Chem. Soc. Rev.* **1998**, *27* (6), 417–425.
- (2) Zhou, H. C.; Long, J. R.; Yaghi, O. M. Introduction to metal-organic frameworks. *Chem. Rev.* **2012**, *112* (2), 673–674.
- (3) Lehn, J. M. Perspectives in chemistry—steps towards complex matter. *Angew. Chem., Int. Ed.* **2013**, *52* (10), 2836–2850.
- (4) Barth, J. V.; Costantini, G.; Kern, K. Engineering atomic and molecular nanostructures at surfaces. *Nature* **2005**, *437*, 671–679.
- (5) Duhm, S.; Heimel, G.; Salzmann, I.; Glowatzki, H.; Johnson, R. L.; Vollmer, A.; Rabe, J. P.; Koch, N. Orientation-dependent ionization energies and interface dipoles in ordered molecular assemblies. *Nat. Mater.* **2008**, *7* (4), 326–332.
- (6) Chen, W.; Qi, D. C.; Huang, H.; Gao, X.; Wee, A. T. Organic-organic heterojunction interfaces: Effect of molecular orientation. *Adv. Funct. Mater.* **2011**, *21* (3), 410–424.
- (7) Breuer, T.; Witte, G. Diffusion-controlled growth of molecular heterostructures: fabrication of two-, one-, and zero-dimensional C₆₀ nanostructures on pentacene substrates. *ACS Appl. Mater. Interfaces* **2013**, *5* (19), 9740–9745.
- (8) Gruenewald, M.; Sauer, C.; Peuker, J.; Meissner, M.; Sojka, F.; Schöll, A.; Reinert, F.; Forker, R.; Fritz, T. Commensurism at electronically weakly interacting phthalocyanine/PTCDA heterointerfaces. *Phys. Rev. B: Condens. Matter Mater. Phys.* **2015**, *91* (15), 155432.
- (9) Stadtmüller, B.; Willenbockel, M.; Schröder, S.; Kleimann, C.; Reinisch, E. M.; Ules, T.; Soubatch, S.; Ramsey, M. G.; Tautz, F. S.; Kumpf, C. Modification of the PTCDA-Ag bond by forming a heteromolecular bilayer film. *Phys. Rev. B: Condens. Matter Mater. Phys.* **2015**, *91* (15), 155433.
- (10) Goiri, E.; Borghetti, P.; El-Sayed, A.; Ortega, J. E.; de Oteyza, D. G. Multi-component organic layers on metal substrates. *Adv. Mater.* **2016**, *28* (7), 1340–1368.
- (11) Wu, B.; Zhao, Y.; Nan, H.; Yang, Z.; Zhang, Y.; Zhao, H.; He, D.; Jiang, Z.; Liu, X.; Li, Y.; Shi, Y.; Ni, Z.; Wang, J.; Xu, J.-B.; Wang, X. Precise, self-limited epitaxy of ultrathin organic semiconductors and heterojunctions tailored by van der Waals interactions. *Nano Lett.* **2016**, *16* (6), 3754–3759.
- (12) Wieghold, S.; Li, J.; Simon, P.; Krause, M.; Avlasevich, Y.; Li, C.; Garrido, J. A.; Heiz, U.; Samori, P.; Müllen, K.; Esch, F.; Barth, J. V.; Palma, C.-A. Photoreponse of supramolecular self-assembled networks on graphene–diamond interfaces. *Nat. Commun.* **2016**, *7*, 10700.
- (13) Pfeiffer, C. R.; Pearce, N.; Champness, N. R. Complexity of two-dimensional self-assembled arrays at surfaces. *Chem. Commun.* **2017**, *53* (84), 11528–11539.
- (14) Jariwala, D.; Marks, T. J.; Hersam, M. C. Mixed-dimensional van der Waals heterostructures. *Nat. Mater.* **2017**, *16* (2), 170–181.
- (15) Gobbi, M.; Bonacchi, S.; Lian, J. X.; Vercouter, A.; Bertolazzi, S.; Zyska, B.; Timpel, M.; Tatti, R.; Olivier, Y.; Hecht, S.; Nardi, M. V.; Beljonne, D.; Orgiu, E.; Samori, P. Collective molecular switching in hybrid superlattices for light-modulated two-dimensional electronics. *Nat. Commun.* **2018**, *9* (1), 2661.
- (16) Guo, L. a.; Wang, Y.; Kaya, D.; Palmer, R. E.; Chen, G.; Guo, Q. Orientational epitaxy of Van der Waals molecular heterostructures. *Nano Lett.* **2018**, *18* (8), 5257–5261.
- (17) Mena-Osteritz, E.; Bäuerle, P. Complexation of C₆₀ on a cyclotriophene monolayer template. *Adv. Mater.* **2006**, *18* (4), 447–451.
- (18) Takami, T.; Arnold, D. P.; Fuchs, A. V.; Will, G. D.; Goh, R.; Waclawik, E. R.; Bell, J. M.; Weiss, P. S.; Sugiura, K.-I.; Liu, W.; Jiang, J. Two-dimensional crystal growth and stacking of bis(phthalocyaninato) rare earth sandwich complexes at the 1-phenyloctane/graphite interface. *J. Phys. Chem. B* **2006**, *110* (4), 1661–1664.
- (19) Blunt, M. O.; Russell, J. C.; Gimenez-Lopez, M. D.; Taleb, N.; Lin, X. L.; Schröder, M.; Champness, N. R.; Beton, P. H. Guest-induced growth of a surface-based supramolecular bilayer. *Nat. Chem.* **2011**, *3* (1), 74–78.
- (20) Ćija, D.; Auwärter, W.; Vijayaraghavan, S.; Seufert, K.; Bischoff, F.; Tashiro, K.; Barth, J. V. Assembly and Manipulation of Rotatable Cerium Porphyrinato Sandwich Complexes on a Surface. *Angew. Chem., Int. Ed.* **2011**, *50* (17), 3872–3877.
- (21) Ciesielski, A.; Cadeddu, A.; Palma, C.-A.; Gorczyński, A.; Patroniak, V.; Cecchini, M.; Samori, P. Self-templating 2D supramolecular networks: a new avenue to reach control over a bilayer formation. *Nanoscale* **2011**, *3* (10), 4125–4129.
- (22) Li, J.; Wieghold, S.; Öner, M. A.; Simon, P.; Hauf, M. V.; Margapoti, E.; Garrido, J. A.; Esch, F.; Palma, C.-A.; Barth, J. V. Three-dimensional bicomponent supramolecular nanoporous self-assembly on a hybrid all-carbon atomically flat and transparent platform. *Nano Lett.* **2014**, *14* (8), 4486–4492.
- (23) Ferreira, Q.; Bragança, A. M.; Alcácer, L.; Morgado, J. Conductance of well-defined porphyrin self-assembled molecular wires up to 14 nm in length. *J. Phys. Chem. C* **2014**, *118* (13), 7229–7234.
- (24) Zheng, Q. N.; Liu, X. H.; Liu, X. R.; Chen, T.; Yan, H. J.; Zhong, Y. W.; Wang, D.; Wan, L. J. Bilayer molecular assembly at a solid/liquid interface as triggered by a mild electric field. *Angew. Chem., Int. Ed.* **2014**, *53* (49), 13395–13399.
- (25) Serrano, G.; Wiespointner-Baumgarthuber, S.; Tebi, S.; Klyatskaya, S.; Ruben, M.; Koch, R.; Müllegger, S. Bilayer of terbium double-decker single-molecule magnets. *J. Phys. Chem. C* **2016**, *120* (25), 13581–13586.
- (26) Cojal González, J. D.; Iyoda, M.; Rabe, J. P. Templated bilayer self-assembly of fully conjugated π -expanded macrocyclic oligothiophenes complexed with fullerenes. *Nat. Commun.* **2017**, *8*, 14717.
- (27) Cui, D.; Ebrahimi, M.; Rosei, F.; Macleod, J. M. Control of fullerene crystallization from 2D to 3D through combined solvent and template effects. *J. Am. Chem. Soc.* **2017**, *139* (46), 16732–16740.
- (28) Hellerstedt, J.; Cahlik, A.; Švec, M.; de la Torre, B.; Morolagares, M.; Chutora, T.; Papoušková, B.; Zoppellaro, G.; Mutombo, P.; Ruben, M.; Zbořil, R.; Jelinek, P. On-surface structural and electronic properties of spontaneously formed Tb₂Pc₃ single molecule magnets. *Nanoscale* **2018**, *10* (33), 15553–15563.
- (29) Urgel, J. I.; Ćija, D.; Vijayaraghavan, S.; Pörtner, M.; Bocquet, M. L.; Auwärter, W.; Barth, J. V. In-situ growth of gadolinium phthalocyaninato sandwich complexes on the Ag (111) surface. *ChemPhysChem* **2019**, *20* (18), 2301–2304.
- (30) Shekha, O.; Wang, H.; Kowarik, S.; Schreiber, F.; Paulus, M.; Tolan, M.; Sternemann, C.; Evers, F.; Zacher, D.; Fischer, R. A.; Wöll, C. Step-by-step route for the synthesis of metal-organic frameworks. *J. Am. Chem. Soc.* **2007**, *129* (49), 15118–15119.
- (31) Bétard, A.; Fischer, R. A. Metal-organic framework thin films: From fundamentals to applications. *Chem. Rev.* **2012**, *112* (2), 1055–1083.
- (32) Korolkov, V. V.; Baldoni, M.; Watanabe, K.; Taniguchi, T.; Besley, E.; Beton, P. H. Supramolecular heterostructures formed by sequential epitaxial deposition of two-dimensional hydrogen-bonded arrays. *Nat. Chem.* **2017**, *9* (12), 1191.
- (33) Decher, G. Fuzzy nanoassemblies: Toward layered polymeric multicomposites. *Science* **1997**, *277* (5330), 1232–1237.
- (34) Stassen, I.; De Vos, D.; Ameloot, R. Vapor-phase deposition and modification of metal-organic frameworks: State-of-the-art and future directions. *Chem. - Eur. J.* **2016**, *22* (41), 14452–14460.
- (35) Liu, J.; Wöll, C. Surface-supported metal-organic framework thin films: fabrication methods, applications, and challenges. *Chem. Soc. Rev.* **2017**, *46* (19), 5730–5770.
- (36) Redhead, P. Thermal desorption of gases. *Vacuum* **1962**, *12* (4), 203–211.
- (37) Zacharia, R.; Ulbricht, H.; Hertel, T. Interlayer cohesive energy of graphite from thermal desorption of polyaromatic hydrocarbons. *Phys. Rev. B: Condens. Matter Mater. Phys.* **2004**, *69* (15), 155406.

- (38) Smith, R. S.; Kay, B. D. Desorption kinetics of benzene and cyclohexane from a graphene surface. *J. Phys. Chem. B* **2018**, *122* (2), 587–594.
- (39) Weippert, J.; Hauns, J.; Bachmann, J.; Böttcher, A.; Yao, X.; Yang, B.; Narita, A.; Müllen, K.; Kappes, M. M. A TPD-based determination of the graphite interlayer cohesion energy. *J. Chem. Phys.* **2018**, *149* (19), 194701.
- (40) King, D. A. Thermal desorption from metal surfaces: A review. *Surf. Sci.* **1975**, *47* (1), 384–402.
- (41) Williams, F. J.; Vaughan, O. P. H.; Knox, K. J.; Bampas, N.; Lambert, R. M. First observation of capping/uncapping by a ligand of a Zn porphyrin adsorbed on Ag(100). *Chem. Commun.* **2004**, *15*, 1688–1689.
- (42) Heinrich, B. W.; Ahmadi, G.; Müller, V. L.; Braun, L.; Pascual, J. I.; Franke, K. J. Change of the Magnetic Coupling of a Metal-Organic Complex with the Substrate by a Stepwise Ligand Reaction. *Nano Lett.* **2013**, *13* (10), 4840–4843.
- (43) Wende, H.; Bernien, M.; Luo, J.; Sorg, C.; Ponpandian, N.; Kurde, J.; Miguel, J.; Piantek, M.; Xu, X.; Eckhold, P.; Kuch, W.; Baberschke, K.; Panchmatia, P. M.; Sanyal, B.; Oppeneer, P. M.; Eriksson, O. Substrate-induced magnetic ordering and switching of iron porphyrin molecules. *Nat. Mater.* **2007**, *6* (7), 516–520.
- (44) Gopakumar, T. G.; Tang, H.; Morillo, J.; Berndt, R. Transfer of Cl ligands between adsorbed iron tetraphenylporphyrin molecules. *J. Am. Chem. Soc.* **2012**, *134* (29), 11844–11847.
- (45) Heinrich, B. W.; Braun, L.; Pascual, J. I.; Franke, K. J. Tuning the magnetic anisotropy of single molecules. *Nano Lett.* **2015**, *15* (6), 4024–4028.
- (46) Feulner, P.; Menzel, D. Simple ways to improve “flash desorption” measurements from single crystal surfaces. *J. Vac. Sci. Technol.* **1980**, *17* (2), 662–663.
- (47) Romberg, R.; Frigo, S. P.; Ogurtsov, A.; Feulner, P.; Menzel, D. Photon stimulated desorption of neutral hydrogen atoms from condensed water and ammonia by resonant O1s and N1s excitation: search for the signature of ultrafast bond breaking. *Surf. Sci.* **2000**, *451* (1–3), 116–123.
- (48) Nečas, D.; Klapetek, P. Gwyddion: an open-source software for SPM data analysis. *Open Phys.* **2012**, *10* (1), 181–188.
- (49) Grosvenor, A. P.; Kobe, B. A.; Biesinger, M. C.; McIntyre, N. S. Investigation of multiplet splitting of Fe 2p XPS spectra and bonding in iron compounds. *Surf. Interface Anal.* **2004**, *36* (12), 1564–1574.
- (50) Stein, S. E. Mass Spectra. *NIST Chemistry WebBook, NIST Standard Reference Database Number 69*; National Institute of Standards and Technology: Gaithersburg, MD, 20899; retrieved July 23, 2017.
- (51) van Vörden, D.; Lange, M.; Schmuck, M.; Schaffert, J.; Cottin, M. C.; Bobisch, C. A.; Möller, R. Substrate induced dehydrogenation: Transformation of octa-ethyl-porphyrin into tetra-benzo-porphyrin. *J. Chem. Phys.* **2013**, *138*, 211102.
- (52) Williams, C. G.; Wang, M.; Skomski, D.; Tempas, C. D.; Kesmodel, L. L.; Tait, S. L. Dehydrocyclization of peripheral alkyl groups in porphyrins at Cu (100) and Ag (111) surfaces. *Surf. Sci.* **2016**, *653*, 130–137.
- (53) Cirera, B.; Giménez-Agulló, N.; Björk, J.; Martínez-Peña, F.; Martín-Jimenez, A.; Rodríguez-Fernandez, J.; Pizarro, A. M.; Otero, R.; Gallego, J. M.; Ballester, P.; Galan-Mascaros, J. R.; Ecija, D. Thermal selectivity of intermolecular versus intramolecular reactions on surfaces. *Nat. Commun.* **2016**, *7* (1), 1–8.
- (54) Schmid, M.; Zirzmeier, J.; Steinrück, H. P.; Gottfried, J. M. Interfacial interactions of iron(II) tetrapyrrole complexes on Au(111). *J. Phys. Chem. C* **2011**, *115* (34), 17028–17035.
- (55) Scheidt, W. R.; Reed, C. A. Spin-state/stereochemical relationships in iron porphyrins: implications for the hemoproteins. *Chem. Rev.* **1981**, *81* (6), 543–555.
- (56) Hieringer, W.; Flechtner, K.; Kretschmann, A.; Seufert, K.; Auwärter, W.; Barth, J. V.; Görling, A.; Steinrück, H. P.; Gottfried, J. M. The surface trans effect: Influence of axial ligands on the surface chemical bonds of adsorbed metalloporphyrins. *J. Am. Chem. Soc.* **2011**, *133* (16), 6206–6222.
- (57) Deimel, P. S.; Bababrik, R. M.; Wang, B.; Blowey, P. J.; Rochford, L. A.; Thakur, P. K.; Lee, T. L.; Bocquet, M. L.; Barth, J. V.; Woodruff, D. P.; Duncan, D. A.; Allegretti, F. Direct quantitative identification of the “surface trans-effect”. *Chem. Sci.* **2016**, *7* (9), 5647–5656.
- (58) Bhandary, S.; Ghosh, S.; Herper, H.; Wende, H.; Eriksson, O.; Sanyal, B. Graphene as a reversible spin manipulator of molecular magnets. *Phys. Rev. Lett.* **2011**, *107* (25), 257202.
- (59) Isvoranu, C.; Wang, B.; Ataman, E.; Schulte, K.; Knudsen, J.; Andersen, J. N.; Bocquet, M. L.; Schnadt, J. Ammonia adsorption on iron phthalocyanine on Au(111): influence on adsorbate-substrate coupling and molecular spin. *J. Chem. Phys.* **2011**, *134* (11), 114710.
- (60) Isvoranu, C.; Wang, B.; Schulte, K.; Ataman, E.; Knudsen, J.; Andersen, J. N.; Bocquet, M. L.; Schnadt, J. Tuning the spin state of iron phthalocyanine by ligand adsorption. *J. Phys.: Condens. Matter* **2010**, *22* (47), 472002–472006.
- (61) Wäckerlin, C.; Tarafder, K.; Siewert, D.; Girovsky, J.; Hählen, T.; Iacovita, C.; Kleibert, A.; Nolting, F.; Jung, T. A.; Oppeneer, P. M.; Ballav, N. On-surface coordination chemistry of planar molecular spin systems: novel magnetochemical effects induced by axial ligands. *Chem. Sci.* **2012**, *3* (11), 3154–3160.
- (62) Wang, W.; Pang, R.; Kuang, G.; Shi, X.; Shang, X.; Liu, P. N.; Lin, N. Intramolecularly resolved Kondo resonance of high-spin Fe (II)-porphyrin adsorbed on Au (111). *Phys. Rev. B: Condens. Matter Mater. Phys.* **2015**, *91* (4), No. 045440.
- (63) Liu, B.; Fu, H.; Guan, J.; Shao, B.; Meng, S.; Guo, J.; Wang, W. An iron-porphyrin complex with large easy-axis magnetic anisotropy on metal substrate. *ACS Nano* **2017**, *11* (11), 11402–11408.
- (64) Rösel, S. r.; Quanz, H.; Logemann, C.; Becker, J.; Mossou, E.; Cañadillas-Delgado, L.; Caldeweyher, E.; Grimme, S.; Schreiner, P. R. London dispersion enables the shortest intermolecular hydrocarbon H...H contact. *J. Am. Chem. Soc.* **2017**, *139* (22), 7428–7431.
- (65) Powell, C. J. Practical guide for inelastic mean free paths, effective attenuation lengths, mean escape depths, and information depths in x-ray photoelectron spectroscopy. *J. Vac. Sci. Technol., A* **2020**, *38* (2), No. 023209.
- (66) Hourahine, B.; Aradi, B.; Blum, V.; Bonafé, F.; Buccheri, A.; Camacho, C.; Cevallos, C.; Deshayé, M. Y.; Dumitrică, T.; Dominguez, A.; et al. DFTB+, a software package for efficient approximate density functional theory based atomistic simulations. *J. Chem. Phys.* **2020**, *152* (12), 124101.
- (67) Senge, M. O. Chloro (2, 3, 7, 8, 12, 13, 17, 18-octaethylporphyrinato) iron (III). *Acta Crystallogr., Sect. E: Struct. Rep. Online* **2005**, *61* (2), m399–m400.
- (68) Abeykoon, B.; Grenèche, J.-M.; Jeanneau, E.; Chernyshov, D.; Goutaudier, C.; Demessence, A.; Devic, T.; Fateeva, A. Tuning the iron redox state inside a microporous porphyrinic metal organic framework. *Dalton Trans.* **2017**, *46* (2), 517–523.
- (69) Sadewasser, S.; Lux-Steiner, M. C. Correct height measurement in noncontact atomic force microscopy. *Phys. Rev. Lett.* **2003**, *91* (26), 266101.